

Fast Quantum Gates for Neutral Atoms Separated by a Few Tens of Micrometers

Matteo Bergonzoni,^{1,*} Rosario Roberto Riso,^{2,1} and Guido Pupillo^{1,†}

¹*University of Strasbourg and CNRS, CESQ and ISIS (UMR 7006), 67000 Strasbourg, France*

²*Department of Chemistry, Norwegian University of Science and Technology, 7491 Trondheim, Norway*

(Dated: November 26, 2025)

We present a theoretical scheme for a family of fast and high-fidelity two-qubit iSWAP gates between neutral atoms separated by more than $20 \mu\text{m}$, enabled by resonant dipole-dipole spin-exchange interactions between Rydberg states. The protocol harnesses coherent excitation-exchange-deexcitation dynamics between the qubit and the Rydberg states within a single and smooth laser pulse, in the presence of strong dipole-dipole interactions. We utilize optimal control methods to achieve theoretical gate fidelities and durations comparable to blockade-based gates in the presence of relevant noise, while extending the effective interaction range by an order of magnitude. This enables entanglement well beyond the blockade radius, offering a route toward fast, high-connectivity quantum processors.

Neutral atoms trapped in optical tweezers are a leading platform for quantum computing. They feature low-defect arrays of thousands of atoms with arbitrary geometries, qubit states exhibiting coherence times of tens of seconds, and high-fidelity two-qubit gates operating on the hundred-nanosecond timescale. [1–8]. Leading two-qubit gates rely on the Rydberg blockade mechanism, where van der Waals (vdW) interactions $V_{\text{vdW}}(R) \sim R^{-6}$ between Rydberg excited states – with R the interatomic distance – prevent multiple excitations of neighboring atoms. Because of the short-range nature of V_{vdW} , the blockade mechanism remains effective only for interatomic separations up to a few micrometers. Extending the entangling range without compromising speed or fidelity is highly desirable for key applications in quantum computing, including the realization of scalable error-corrected architectures [9, 10]. Currently, entangling atoms over distances in the tens of micrometers range is achieved in experiments via qubit shuttling – i.e. moving the tweezers – on timescales of hundreds of microseconds [10–12]. Alternatively, DC or microwave fields have been used to engineer gates by tuning the Förster defect between selected Rydberg states without moving the atoms, but such schemes are highly sensitive to field fluctuations and atomic positioning [13, 14]. A further strategy employs ancillary atoms to mediate interactions, at the cost of increased atomic overhead and gate times [15–17].

In this work, we propose a family of fast two-qubit gates based on resonant dipolar exchange interaction $J(R) \sim R^{-3}$ [18–23] for atoms separated by tens of micrometers. Our approach relies on excitation and de-excitation from the long-lived qubit manifold – e.g., two hyperfine states of the electronic ground-state – to the Rydberg manifold – where fast resonant exchange dynamics occurs – within a single continuous laser pulse. This method achieves an iSWAP gate between the ground-state qubits on sub-microsecond timescales (Fig. 1). Using quantum optimal control, we propose gates that are both time-optimal and robust against the main error sources, which we identify as vdW interac-

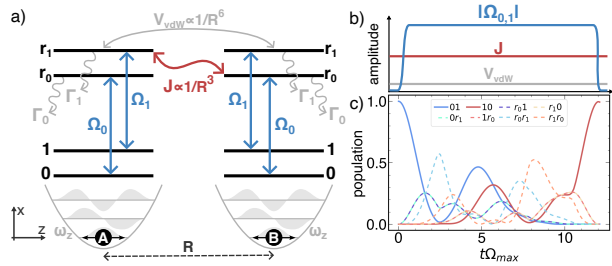


FIG. 1. iSWAP gate with Rydberg atoms. (a) Two atoms separated by a distance R , irradiated by two laser fields $\Omega_{0,1}$, with a resonant dipolar coupling J . Rydberg decay $\Gamma_{0,1}$, atomic motion, and vdW interactions V_{vdW} are also included. (b) A single optimal laser pulse $\Omega_{0,1}$ is applied, with dipolar and vdW interactions present from the outset. (c) Evolution of the two-atom state populations during the pulse for $\Omega_{\max}/J = 2.1$ (Fig. 2(c)), starting from the state $|01\rangle$.

tions, spontaneous emission in the Rydberg manifold, and motion due to photon recoil, dipolar and vdW forces and finite temperature. We achieve theoretical performances in terms of gate speed and fidelity comparable to blockade-based gates but with the interaction range enhanced by almost an order of magnitude. We discuss implications for near term quantum memories and computers.

We consider two atoms, labeled $\alpha = A$ and B , separated by distance R (Fig. 1(a)). Logical states $|0\rangle_\alpha$ and $|1\rangle_\alpha$ are encoded in long-lived ground or metastable states of the atoms. The atoms are simultaneously irradiated by two global fields with Rabi frequency $|\Omega_j(t)|e^{i\phi_j(t)}$, driving the transition $|j\rangle_\alpha \leftrightarrow |r_j\rangle_\alpha$ ($j = 0, 1$), with $|r_0\rangle_\alpha$ and $|r_1\rangle_\alpha$ two Rydberg states. In the basic scheme, the Rydberg states of the two atoms are coupled by the dipolar spin-exchange interaction J , resulting in the following Hamiltonian in the rotating frame

$$H(t) = \sum_{j,\alpha} \frac{|\Omega_j(t)|}{2} \left(e^{i\phi_j(t)} |j\rangle \langle r_j|_\alpha + \text{h.c.} \right) + J (|r_0 r_1\rangle \langle r_1 r_0| + \text{h.c.}), \quad (1)$$

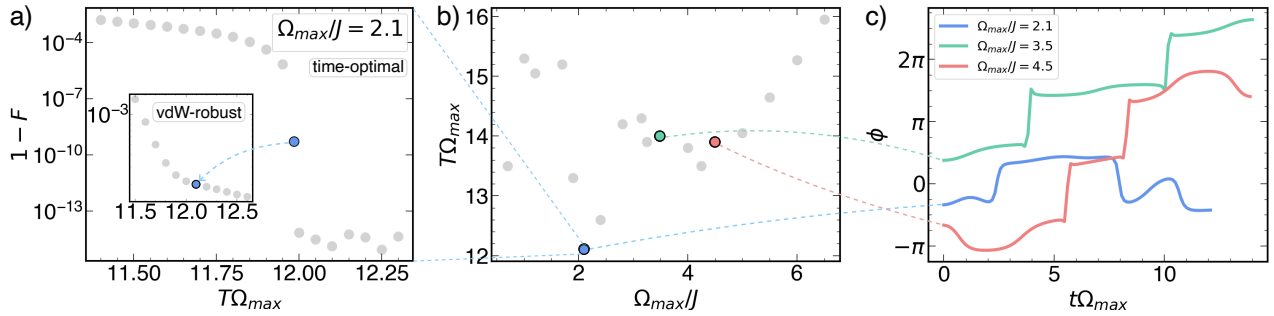


FIG. 2. Time-optimal and vdW-robust pulses. (a) Minimum infidelity $1-F$ found by GRAPE for pulses of different durations T , in units of the Rabi frequency Ω_{\max} , for the given ratio $\Omega_{\max}/J = 2.1$. The time-optimal pulse has duration $T\Omega_{\max} = 11.95$, while trying to make it robust to vdW interactions the pulse durations is increased to $T\Omega_{\max} = 12.1$ (inset). (b) Optimal duration T , in units of Ω_{\max} versus coupling ratio Ω_{\max}/J of the vdW-robust pulses. The resulting duration T , range R , and fidelity F obtained for a realistic choice of experimental parameters are shown in Fig. 3. (c) Optimal phase profile $\phi(t)$ of three vdW-robust pulses.

with $|r_0r_1\rangle \equiv |r_0\rangle_A \otimes |r_1\rangle_B$ and $\hbar = 1$. Equation (1) neglects spontaneous emission, atomic motion, photon recoil, and residual vdW interactions; their impact and possible mitigation strategies are discussed below. Equation (1) allows, in principle, for the implementation of an iSWAP gate $U_{\text{iSWAP}} = |00\rangle\langle 00| + |11\rangle\langle 11| + i(|01\rangle\langle 10| + |10\rangle\langle 01|)$ between the logical states, which, together with single-qubit rotations, provides a complete gate set for quantum computing. The simplest iSWAP implementation, analogous to protocols with polar molecules [24–28], consists of a π pulse that excites the atoms to the Rydberg states, a period of free evolution under J to generate entanglement, and a second π pulse that de-excites them (see Suppl. Mat.). However, unlike in rotational states of polar molecules, in Rydberg systems the dipolar interaction is usually comparable to or larger than the Rabi frequency ($J \gtrsim |\Omega_{0,1}|$), thus perturbing the π -pulse dynamics. In the following, we propose a protocol and concrete examples to realize high-fidelity iSWAP gates with a single continuous pulse scheme – which we determine by optimal control methods – that takes into account these interactions during the laser excitation and de-excitation, as well as all other relevant effects, such as vdW interactions in the excited states, spontaneous emission from the Rydberg states, and atomic motion including photon-recoil effects. Our goal is to demonstrate gates on the tens of μm scale with fidelities compatible with quantum error correction.

As an example, we consider ^{87}Rb , where qubit states can be encoded in the hyperfine levels $|0\rangle_\alpha \equiv |F=1, m_F=0\rangle_\alpha$ and $|1\rangle_\alpha \equiv |F=2, m_F=0\rangle_\alpha$ of the ground state manifold $5S_{1/2}$, with F the total angular momentum and m_F its projection along the quantization (interatomic) axis z . The Rydberg states $nS_{1/2}$ with $m_j = 1/2$ and $nP_{3/2}$ with $m_j = 3/2$ are chosen as $|r_0\rangle_\alpha$ and $|r_1\rangle_\alpha$, respectively, with n the principal quantum number. This results in dipolar interaction energies J in the range $0.1 \lesssim J/2\pi \lesssim 1\text{ GHz}$, for the consid-

ered quantum numbers $n \gtrsim 50$ and interatomic distances $R \sim 3 - 30\text{ }\mu\text{m}$. We consider realistic Rabi frequencies $1 \leq |\Omega_{0,1}|/2\pi \leq 100\text{ MHz}$.

Time-optimal gate.— As a first step, we demonstrate a time-optimal scheme for implementing U_{iSWAP} with Eq. (1), i.e., including only the combined effects of J and the laser drive. Time optimality minimizes spontaneous emission, a fundamental error source for Rydberg atoms [3, 4, 6–8, 29]. As in Rydberg blockade schemes [29–31], we define a cost function $1-F$, with F the Bell state fidelity

$$F = \frac{1}{16} \left| \sum_q \langle \psi_q | R^{\otimes 2} U_{\text{iSWAP}} | q \rangle \right|^2, \quad (2)$$

where $|\psi_q\rangle$ is the actual two-qubit final state obtained by applying the pulse to $|q\rangle$, from the computational basis $|q\rangle \in \{|00\rangle, |01\rangle, |10\rangle, |11\rangle\}$. $|\psi_q\rangle$ is therefore compared to the target state $U_{\text{iSWAP}}|q\rangle$ up to a final global single-qubit operation $R(\theta, \varphi, \lambda) = e^{i(\varphi+\lambda)/2} R_z(\varphi) R_y(\theta) R_z(\lambda)$, where φ , θ , and λ are rotation angles treated as additional optimization parameters. The cost function is numerically minimized using quantum optimal control methods – here we use the GRAPE algorithm [29, 32]. The time-optimal pulse is defined as the shortest pulse that achieves zero infidelity $1-F$, within numerical precision. We apply this approach to a wide range of experimentally relevant ratios $0 \lesssim |\Omega_{0,1}|/J \lesssim 10$.

Our first key result is that, for $0 \lesssim |\Omega_{0,1}|/J \lesssim 10$ time-optimal pulses are those for which the amplitudes of the two Rabi frequencies are equal to the maximum available Rabi frequency in experiments, which here we assume identical for the two lasers, i.e., $|\Omega_0(t)| = |\Omega_1(t)| = \Omega_{\max}$. In addition, we find that time optimality also requires same lasers phases, i.e., $\phi_0(t) = \phi_1(t) = \phi(t)$, with $\phi(t)$ the key variable to be varied in time to minimize $1-F$, which has not been done before. Figure 2(a) shows an example result of the infidelity $1-F$ versus the

Noise term		No noise \emptyset	vdW H_{vdW}	Decay H_Γ	z -motion $H_J^{(1,z)} + H_{\text{vdW}}^{(1,z)}$	Recoil (detuning)		Recoil (coupling)		All $\bar{\ell} = z$
						$\Delta_j = 0$	$\Delta_j = -\frac{2\pi^2}{m\lambda_j^2}$	$\bar{\ell} = x$	$\bar{\ell} = z$	
1 - F	TO	7.0×10^{-6}	1.3×10^{-2}	7.0×10^{-4}	4.3×10^{-5}	1.3×10^{-5}	$< 10^{-7}$	2.3×10^{-5}	4.9×10^{-5}	1.3×10^{-2}
	vdW-R	-	2.0×10^{-4}	7.0×10^{-4}	3.7×10^{-5}	8.7×10^{-6}	$< 10^{-7}$	1.9×10^{-5}	5.1×10^{-5}	9.9×10^{-4}

TABLE I. Error budget of the time-optimal (TO) and van der Waals-robust (vdW-R) pulses for $\Omega_{\text{max}}/J = 2.1$. Reported are infidelities $1 - F$ in the absence of perturbations and in the presence of individual perturbations, namely vdW interactions, Rydberg decay, atomic motion along the interatomic z axis, and photon recoil – considering both its effects: detuning (compensated and uncompensated) and coupling between internal and motional states (for laser orientations along x and z). Experimental parameters used in the simulations: Rabi frequency $\Omega_{\text{max}}/2\pi = 10$ MHz, principal quantum number $n = 100$ of ^{87}Rb , trapping frequencies $\omega_z/2\pi = 100$ kHz, $\omega_x = \omega_z/5$ and temperature $T_{\text{temp}} = 1$ μK .

total gate duration T for a given ratio $\Omega_{\text{max}}/J = 2.1$, with T in units of Ω_{max} . The figure shows that the infidelity decreases abruptly to numerical zero around $T\Omega_{\text{max}} = 11.95$ (blue dot), corresponding to the time-optimal pulse. Varying the ratio Ω_{max}/J results in different optimal phase profiles and gate durations, with the shortest pulse obtained for $\Omega_{\text{max}}/J = 0.7$, corresponding to $T\Omega_{\text{max}} = 8.2$. This is essentially the same timescale of the time-optimal blockade gate ($T\Omega_{\text{max}} = 7.5$) [29] or the recently proposed short-range resonant dipole-dipole CZ gate ($T\Omega_{\text{max}} = 5.95$) [23]. However, here the range of the gate scales as $R \sim \sqrt[3]{n^4(\Omega_{\text{max}}/J)/\Omega_{\text{max}}}$, which allows to reach distances of tens of micrometers. For example, for $\Omega_{\text{max}}/2\pi = 10$ MHz, $\Omega_{\text{max}}/J = 2.1$ and $n = 100$, we obtain $R = 20$ μm . We find that the dependence of the optimal T vs Ω_{max}/J is not monotonic (see Suppl. Mat.), however in general it tends to increase with increasing Ω_{max}/J . This would appear to favor shorter pulses, which minimize spontaneous emission. However, shorter pulses are more affected by atomic motion and vdW interactions, and thus do not necessarily represent the optimal solution in realistic situations, which we address next.

Imperfections and robustness – The relevant Hamiltonian to realize robust U_{iSWAP} gates with Rydberg atoms beyond Eq. (1) reads $H' = H'_\Omega + H'_J + H'_{\text{vdW}} + H_K + H_\Gamma$, with

$$\begin{aligned}
H'_\Omega &= \sum_{j,\alpha} \frac{\Omega_j}{2} \left[e^{i\phi_j + i\eta_j(a_{\bar{\ell},\alpha} + a_{\bar{\ell},\alpha}^\dagger)} |j\rangle \langle r_j|_\alpha + \text{h.c.} \right] \\
H'_J &= J \left[1 - 3 \frac{z_A - z_B}{R} \right] (|r_0 r_1\rangle \langle r_1 r_0| + \text{h.c.}) \\
H'_{\text{vdW}} &= \sum_{i,j} V_{ij} \left[1 - 6 \frac{z_A - z_B}{R} \right] |r_i r_j\rangle \langle r_i r_j| \\
H_K &= - \sum_{\alpha,\ell} \frac{p_{\alpha,\ell}^2}{2m}, \quad H_\Gamma = -\frac{i}{2} \sum_{j,\alpha} \Gamma_j |r_j\rangle \langle r_j|_\alpha. \quad (3)
\end{aligned}$$

The term H'_Ω in Eq. (3) includes the effect of photon recoil in the laser driving Hamiltonian, characterized by the Lamb-Dicke parameter η_j , and with $a_{\bar{\ell},\alpha}^\dagger$ and $a_{\bar{\ell},\alpha}$ the ladder operators for the harmonic trap of atom α along

the laser propagation direction $\bar{\ell}$ [23, 33]. The term H'_J includes the first-order correction in the dipole-dipole interaction J of Eq. (1), arising from atomic motion along the interatomic direction z , where z_α is the position operator of atom α in its radial harmonic trap (see Suppl. Mat.). H'_{vdW} describes off-resonant van der Waals interactions and their first-order position-dependent corrections $H_{\text{vdW}}^{(1,z)}$ in the z direction. H_K is the kinetic operator, with m the atomic mass and $p_{\alpha,\ell}$ the momentum operator of atom α along the three axis $\ell = x, y, z$. The trapping potential is here omitted as optical tweezers are usually turned off during the Rydberg excitation pulses [3, 34]. Finally, H_Γ in Eq. (3) is a non-Hermitian term describing decay from Rydberg states with rates $\Gamma_{0,1}$.

Photon recoil has a twofold effect: First, it introduces a constant detuning $\Delta_j = 2\pi^2/(m\lambda_j^2)$ corresponding to the kinetic energy imparted by a photon of laser j , with wavelength λ_j . Second, it induces a coupling between motional degrees of freedom along the $\bar{\ell}$ direction and the internal states of the atom, with strength $\sim \sqrt{\omega_{\bar{\ell}}/(m\lambda_j^2)}$ and with $\omega_{\bar{\ell}}$ the trapping frequency in the laser direction (see Suppl. Mat.). This results in decoherence of the internal states by entanglement of motional and electronic states. H'_J results in further coupling between motional degrees of freedom and internal states of the atom – with coupling strength $\sim J/(R\sqrt{m\omega_z})$ – due to quantum mechanical motional spread of the wavefunctions. Similar effects are observed for van der Waals interactions H_{vdW} .

Table I provides an example of error budget resulting from the terms in Eq. (3) for the time-optimal (TO) pulse with $\Omega_{\text{max}}/J = 2.1$, for a choice of realistic experimental parameters. The table shows that vdW interactions largely dominate the error budget, accounting for an infidelity $1 - F \sim 10^{-2}$, while all other error sources provide orders of magnitude smaller contributions (see Suppl. Mat. for details of the calculations).

In this work, we therefore proceed to obtain high-fidelity gates $1 - F < 10^{-3}$ by making the TO pulses robust against vdW interactions. This is achieved by including the latter directly in the optimization, using the TO pulses as initial guess. In general, for small ratios $\Omega_{\text{max}}/J \lesssim 1$ – corresponding to smaller inter-

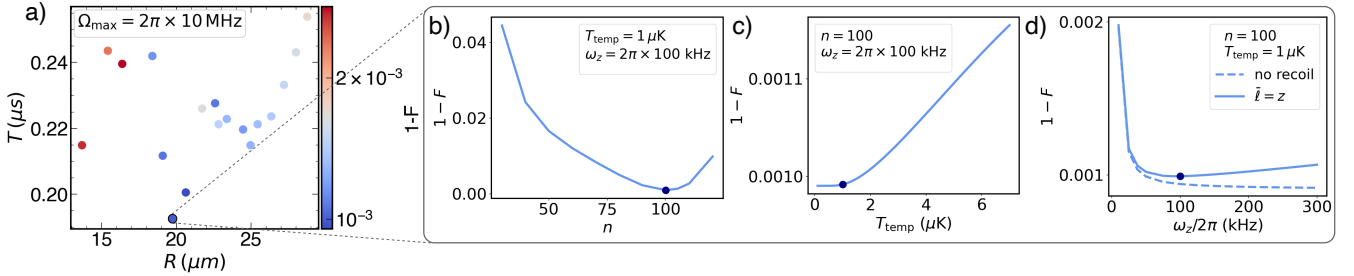


FIG. 3. Infidelity of the vdW-robust pulses for a fixed Rabi frequency $\Omega_{\text{max}}/2\pi = 10 \text{ MHz}$. (a) Heat map of gate infidelity $1-F$ (color scale on the right) for several coupling ratios Ω_{max}/J , with $1.5 \leq J \leq 15 \text{ MHz}$. (b)-(d) Fidelity of the vdW-robust pulse for $\Omega_{\text{max}}/J = 2.1$ as a function of (b) the principal quantum number n , (c) the atomic temperature T_{temp} , and (d) the radial trapping frequency $\omega_z/2\pi$, in absence of photon recoil and with the laser orientated along the interatomic direction ($\ell = z$).

atomic distances R – the numerical optimization fails to find a robust pulse with a duration T comparable to the TO one. For larger ratios $\Omega_{\text{max}}/J \gtrsim 3$, however, we find pulses with high fidelity while maintaining almost the same pulse duration, as a result of the short-range nature of vdW interactions. Figure 2(b) shows the minimum vdW-robust gate duration T as a function of Ω_{max}/J : For $\Omega_{\text{max}}/J = 2.1$, the robust pulse duration is $T\Omega_{\text{max}} = 12.1$. This is less than 2% longer than the corresponding TO pulse (see Fig. 2(a)), but with infidelity well below 10^{-3} in the presence of vdW interactions only. Increasing the duration T of the robust pulse can further decrease the infidelity (see inset in Fig. 2(a)). Figure 2(c) plots the optimal phase $\phi(t)$ for three representative pulses: In all cases, the pulses are smooth in time, which should make them easier to implement in experiments. Jumps of π in the phase for $\Omega_{\text{max}}/J > 2.1$ can in principle be removed by re-optimizing the pulse for the detuning – instead of the phase only – and fixing a cutoff, with minimal loss of pulse performance [35].

Figure 3(a) analyzes of a set of vdW-robust pulses for different values of the ratio Ω_{max}/J , including all terms in Eq. (3). The pulse with $\Omega_{\text{max}}/J = 2.1$, assuming a Rabi frequency $\Omega_{\text{max}}/2\pi = 10 \text{ MHz}$, radial trapping frequency $\omega_z/2\pi = 100 \text{ kHz}$, temperature $T_{\text{temp}} = 1 \mu\text{K}$, and principal quantum number $n = 100$ of ^{87}Rb , yields an infidelity $1-F < 1 \times 10^{-3}$, at an interatomic distance $R = 20 \mu\text{m}$ and with total pulse duration $T = 190 \text{ ns}$, which is comparable to that of CZ gates based on the blockade mechanism [3, 4, 29]. To cover the same distance the state-of-the-art qubit transport would require times that are three orders of magnitude longer [10]. The fidelity remains high, $1-F \leq 2 \times 10^{-3}$, even for larger ratios $\Omega_{\text{max}}/J \lesssim 7$, allowing the implementation of entangling pulses between even more distant atoms, $R \approx 30 \mu\text{m}$, on sub- μs timescales.

In Figs. 3(b)-(d), the fidelity of the robust pulse $\Omega_{\text{max}}/J = 2.1$ is analyzed as a function of the principal quantum number n , the temperature T_{temp} and the radial trapping frequency ω_z . Increasing n shortens the pulse duration, since $J \sim n^4$, and increases the Ryd-

berg lifetime $\Gamma \sim n^{-3}$, thus reducing the infidelity. This is the case, provided that the pulse is optimized to remain robust against the corresponding vdW interactions; otherwise, a larger n amplifies their perturbative effect $V_{\text{vdW}} \sim n^{11}$ (see Fig. 3(b)). The improvement in infidelity is partially reduced by the decrease of the Rabi frequency $\Omega_{\text{max}} \sim n^{-3/2}$ [1]. Lower temperatures decrease the occupation of excited motional states and thus position uncertainty (see Fig. 3(c)). Finally, the trapping frequency also plays a crucial role. The displacement operator scales as $1/\sqrt{\omega_z}$, whereas the momentum kick effect grows as $\sqrt{\omega_{\ell}}$. If the lasers are aligned in the interatomic direction $\ell = z$, there is a trade-off between position fluctuation and photon recoil leading to an optimal confinement near $\omega_z^* \approx 90 \text{ kHz}$ from the balance between these competing effects (see solid line in Fig. 3(d)). This is a well known effect, already documented in Refs. [22, 23, 30, 33]. If, instead, the lasers are oriented along the more weakly confined axial direction $\ell = x$, with typically $\omega_z \approx 5\omega_x$, the effects of photon recoil are suppressed, and the optimal confinement becomes much larger (see dashed line in Fig. 3(d)).

Conclusion.— In summary, we have demonstrated a protocol for time-optimal, high-fidelity iSWAP gates between neutral atoms separated by tens of micrometers. The scheme combines resonant dipolar spin-exchange interactions with optimally shaped laser pulses, yielding gate speeds comparable to the fastest CZ gates at few- μm distances. The achieved fidelities are compatible with thresholds for error correction [36], and further improvements can be realized by mitigating residual errors detailed in Table I. In particular, recoil-induced detuning can be compensated by fine-tuning the laser frequency, and motional-electronic coupling can be reduced by aligning the beams along the weakly confined axial direction. Heavier atomic species, such as ^{133}Cs , further suppress motional errors.

These results open several promising research directions. This approach could be extended to realize k -qubit gates ($k > 2$) via resonant dipole-dipole interactions, enhancing stabilizer efficiency in quantum error-correcting

codes [37, 38] while reducing gate count and circuit depth [39]. In particular, the fast, long-range gates introduced here can enable efficient quantum information transport across neutral-atom registers without intermediate operations, ancillary qubits, or atomic motion—an essential capability for fast, modular quantum computing and error correction. Moreover, these high-fidelity gates may facilitate the implementation of recently developed low-density parity-check (LDPC) codes, which require stabilizer qubits separated by large distances [38, 40–43]. Exploiting long-range interactions, such codes can achieve higher encoding rates, reduced qubit overhead, and larger code distances d , yielding lower logical error probabilities than surface codes of comparable size.

Acknowledgments.— We are grateful to S. Whitlock for insightful discussions. This research has received funding from the European Union’s Horizon Europe programme HORIZON-CL4-2021-DIGITAL-EMERGING-01-30 via the project 101070144 (EuRyQa) and from the French National Research Agency under the Investments of the Future Program projects ANR-21-ESRE-0032 (aQCess), ANR-22-CE47-0013-02 (CLIMAQS), and ANR-22-CMAM-0001 France 2030 (QuanTEdu-France). See Suppl. Mat. for details on the optimization algorithm, motion simulation, and fidelity function.

E. Megidish, M. Meredith, M. McDonald, R. Morshed, S. Narayanaswami, C. Nishiguchi, T. Paule, K. A. Pawlak, K. L. Pudenz, D. R. Pérez, A. Ryou, J. Simon, A. Smull, M. Urbanek, R. J. M. van de Veerdonk, Z. Vendeiro, T.-Y. Wu, X. Xie, and B. J. Bloom, *PRX Quantum* **6**, 020334 (2025).

- [9] M. Morgado and S. Whitlock, *AVS Quantum Science* **3**, 023501 (2021).
- [10] M. Saffman, *Quantum computing with atomic qubit arrays: confronting the cost of connectivity* (2025), arXiv:2505.11218 [quant-ph].
- [11] G. Pichard, D. Lim, E. Bloch, J. Vaneechoutte, L. Bourachot, G.-J. Both, G. Mériaux, S. Dutartre, R. Hostein, J. Paris, B. Ximenez, A. Signoles, A. Browaeys, T. Lahaye, and D. Dreon, *Phys. Rev. Appl.* **22**, 024073 (2024).
- [12] H. Zhou, C. Zhao, M. Cain, D. Bluvstein, N. Maskara, C. Duckering, H.-Y. Hu, S.-T. Wang, A. Kubica, and M. D. Lukin, *Nature* **646**, 303 (2025).
- [13] I. N. Ashkarin, S. Lepoutre, P. Pillet, I. I. Beterov, I. I. Ryabtsev, and P. Cheinet, *Phys. Rev. Res.* **7**, 013034 (2025).
- [14] D. Kurdak, P. R. Banner, Y. Li, S. R. Muleady, A. V. Gorshkov, S. L. Rolston, and J. V. Porto, *Phys. Rev. Lett.* **134**, 123404 (2025).
- [15] A. Cesa and J. Martin, *Phys. Rev. A* **95**, 052330 (2017).
- [16] Y. Sun, *Science China Physics, Mechanics & Astronomy* **67**, 120311 (2024).
- [17] G. Doultinos and D. Petrosyan, *Phys. Rev. Res.* **7**, 023246 (2025).
- [18] A. Reinhard, T. C. Liebisch, B. Knuffman, and G. Raithel, *Phys. Rev. A* **75**, 032712 (2007).
- [19] S.-L. Su and W. Li, *Phys. Rev. A* **104**, 033716 (2021).
- [20] Y. Chew, T. Tomita, T. P. Mahesh, S. Sugawa, S. de Léséleuc, and K. Ohmori, *Nature Photonics* **16**, 724–729 (2022).
- [21] P. Méhaignerie, Y. Machu, A. Durán Hernández, G. Creutzer, D. Papoulier, J. Raimond, C. Sayrin, and M. Brune, *PRX Quantum* **6**, 10.1103/prxquantum.6.010353 (2025).
- [22] G. Emperaiger, M. Qiao, G. Bornet, C. Chen, R. Martin, Y. T. Chew, B. Gély, L. Klein, D. Barredo, A. Browaeys, and T. Lahaye, *Phys. Rev. A* **111**, 062806 (2025).
- [23] G. Giudici, S. Veroni, G. Giudice, H. Pichler, and J. Zeiher, *PRX Quantum* **6**, 030308 (2025).
- [24] K.-K. Ni, T. Rosenband, and D. D. Grimes, *Chem. Sci.* **9**, 6830 (2018).
- [25] C. M. Holland, Y. Lu, and L. W. Cheuk, *Science* **382**, 1143 (2023).
- [26] Y. Bao, S. S. Yu, L. Anderegg, E. Chae, W. Ketterle, K.-K. Ni, and J. M. Doyle, *Science* **382**, 1138 (2023).
- [27] L. R. B. Picard, A. J. Park, G. E. Patenotte, S. Gebretsadkan, D. Wellnitz, A. M. Rey, and K.-K. Ni, *Nature* **637**, 821 (2025).
- [28] D. K. Ruttle, T. R. Hepworth, A. Guttridge, and S. L. Cornish, *Nature* **637**, 827 (2025).
- [29] S. Jandura and G. Pupillo, *Quantum* **6**, 712 (2022).
- [30] A. Pagano, S. Weber, D. Jaschke, T. Pfau, F. Meinert, S. Montangero, and H. P. Büchler, *Phys. Rev. Res.* **4**, 033019 (2022).
- [31] M. Mohan, R. de Keijzer, and S. Kokkelmans, *Phys. Rev. Res.* **5**, 033052 (2023).
- [32] N. Khaneja, T. Reiss, C. Kehlet, T. Schulte-Herbrüggen, and S. J. Glaser, *Journal of Magnetic Resonance* **172**, 296 (2005).

* bergonzoni@unistra.fr

† pupillo@unistra.fr

- [1] M. Saffman, T. G. Walker, and K. Mølmer, *Rev. Mod. Phys.* **82**, 2313 (2010).
- [2] M. Schlosser, S. Tichelmann, D. Schäffner, D. O. de Mello, M. Hambach, J. Schütz, and G. Birk, *Phys. Rev. Lett.* **130**, 180601 (2023).
- [3] S. J. Evered, D. Bluvstein, M. Kalinowski, S. Ebadi, T. Manovitz, H. Zhou, S. H. Li, A. A. Geim, T. T. Wang, N. Maskara, H. Levine, G. Semeghini, M. Greiner, V. Vuletić, and M. D. Lukin, *Nature* **622**, 268–272 (2023).
- [4] S. Ma, G. Liu, P. Peng, B. Zhang, S. Jandura, J. Claes, A. P. Burgers, G. Pupillo, S. Puri, and J. D. Thompson, *Nature* **622**, 279–284 (2023).
- [5] W.-X. Li, J.-L. Wu, S.-L. Su, and J. Qian, *Phys. Rev. A* **109**, 012608 (2024).
- [6] R. B.-S. Tsai, X. Sun, A. L. Shaw, R. Finkelstein, and M. Endres, *PRX Quantum* **6**, 010331 (2025).
- [7] M. Peper, Y. Li, D. Y. Knapp, M. Bileska, S. Ma, G. Liu, P. Peng, B. Zhang, S. P. Horvath, A. P. Burgers, and J. D. Thompson, *Phys. Rev. X* **15**, 011009 (2025).
- [8] J. A. Muniz, M. Stone, D. T. Stack, M. Jaffe, J. M. Kindem, L. Wadleigh, E. Zalys-Geller, X. Zhang, C.-A. Chen, M. A. Norcia, J. Epstein, E. Halperin, F. Hummel, T. Wilkason, M. Li, K. Barnes, P. Battaglino, T. C. Bohdanowicz, G. Booth, A. Brown, M. O. Brown, W. B. Cairncross, K. Cassella, R. Coxe, D. Crow, M. Feldkamp, C. Griger, A. Heinz, A. M. W. Jones, H. Kim, J. King, K. Kotru, J. Lauigan, J. Marjanovic,

- [33] F. Robicheaux, T. M. Graham, and M. Saffman, *Phys. Rev. A* **103**, 022424 (2021).
- [34] Z. Zuo, M. Fukusen, Y. Tamaki, T. Watanabe, Y. Nakagawa, and K. Nakagawa, *Opt. Express* **17**, 22898 (2009).
- [35] L. Pecorari, S. Jandura, and G. Pupillo, *Low-depth quantum error correction via three-qubit gates in rydberg atom arrays* (2025), arXiv:2507.06096 [quant-ph].
- [36] A. G. Fowler, M. Mariantoni, J. M. Martinis, and A. N. Cleland, *Phys. Rev. A* **86**, 032324 (2012).
- [37] J. Old, S. Tasler, M. J. Hartmann, and M. Müller, *Fault-tolerant stabilizer measurements in surface codes with three-qubit gates* (2025), arXiv:2506.09029 [quant-ph].
- [38] L. Pecorari, S. Jandura, G. K. Brennen, and G. Pupillo, *Nature Communications* **16**, 1111 (2025).
- [39] J. M. Baker, A. Litteken, C. Duckering, H. Hoffmann, H. Bernien, and F. T. Chong, in *2021 ACM/IEEE 48th Annual International Symposium on Computer Architecture (ISCA)* (2021) pp. 818–831.
- [40] M. A. Tremblay, N. Delfosse, and M. E. Beverland, *Phys. Rev. Lett.* **129**, 050504 (2022).
- [41] S. Bravyi, A. W. Cross, J. M. Gambetta, D. Maslov, P. Rall, and T. J. Yoder, *Nature* **627**, 778–782 (2024).
- [42] Q. Xu, J. P. Bonilla Ataides, C. A. Pattison, N. Raveendran, D. Bluvstein, J. Wurtz, B. Vasić, M. D. Lukin, L. Jiang, and H. Zhou, *Nature Physics* **20**, 1084 (2024).
- [43] C. Poole, T. M. Graham, M. A. Perlin, M. Otten, and M. Saffman, *Phys. Rev. A* **111**, 022433 (2025).
- [44] M. A. Nielsen and I. L. Chuang, *Quantum Computation and Quantum Information: 10th Anniversary Edition* (Cambridge University Press, 2010).

Supplemental Material for “Fast Quantum Gates for Neutral Atoms Separated by a Few Tens of Micrometers”

Choice of the states

In this work, we consider atoms of Rubidium-87. In the ground state $5S_{1/2}$, the logical states can be encoded in the long-lived hyperfine levels $|0\rangle \equiv |F = 1, m_F = 0\rangle$ and $|1\rangle \equiv |F = 2, m_F = 0\rangle$, where F denotes the total atomic angular momentum and m_F its projection along the quantization axis. The Rydberg states $nS_{1/2}$ with $m_j = 1/2$ and $nP_{3/2}$ with $m_j = 3/2$ are chosen as $|r_0\rangle$ and $|r_1\rangle$, respectively, with $n \gtrsim 50$ the principal quantum number. The choice of n plays an important role in determining both the duration and fidelity of the protocol, since it sets the scaling of the relevant quantities: Rabi frequency $\Omega_{\max} \sim n^{-3/2}$, decay rate $\Gamma \sim n^{-3}$, dipole-dipole and van der Waals (vdW) interaction strengths, $J \sim n^4$ and $V_{\text{vdW}} \sim n^{11}$, respectively [2]. Tables S1 and S2 provide representative examples of the relevant atomic quantities considered in this work, such as the resonant dipole-dipole and van der Waals interaction strengths, J and V_{vdW} , the corresponding dispersion coefficients, C_3 and C_6 , and the decay rates, Γ .

Dipole-dipole interaction

The dipole-dipole interaction $V_{\text{dd}}(\vec{R})$ between two dipoles \vec{d}_α ($\alpha = A, B$) separated by a distance vector \vec{R} reads [3, 4]

$$V_{\text{dd}}(\vec{R}) = \frac{\vec{d}_A \cdot \vec{d}_B - 3(\vec{d}_A \cdot \hat{R})(\vec{d}_B \cdot \hat{R})}{R^3}, \quad (\text{S1})$$

where $R = |\vec{R}|$ is the magnitude of the interdipole separation, and $\hat{R} = \vec{R}/R$ is the corresponding unit vector. The expression in Eq. (S1) can also be rewritten as [3, 5]

$$\begin{aligned} V_{\text{dd}}(\vec{R}) = & \frac{1}{R^3} \left[\frac{1 - 3 \cos^2 \theta}{2} (d_A^{+1} d_B^{-1} + d_A^{-1} d_B^{+1} + 2 d_A^0 d_B^0) \right. \\ & + \frac{3}{\sqrt{2}} \sin \theta \cos \theta ((d_A^{+1} d_B^0 + d_A^0 d_B^{+1}) e^{-i\varphi} - (d_A^{-1} d_B^0 + d_A^0 d_B^{-1}) e^{i\varphi}) \\ & \left. - \frac{3}{2} \sin^2 \theta (d_A^{-1} d_B^{-1} e^{2i\varphi} + d_A^{+1} d_B^{+1} e^{-2i\varphi}) \right], \end{aligned} \quad (\text{S2})$$

where the separation vector \vec{R} has been expressed in spherical coordinates as $\vec{R} = R(\sin \theta \cos \varphi, \sin \theta \sin \varphi, \cos \theta)$, with θ the polar angle between \vec{R} and the z axis, and φ the azimuthal angle. The dipole moment operators $\vec{d}_\alpha = (d_\alpha^x, d_\alpha^y, d_\alpha^z)$

n	R (μm)	$J/2\pi$ (MHz)	V_{00}/J	V_{01}/J	V_{11}/J
50	10	2.05	7.5×10^{-3}	1.5×10^{-3}	6.0×10^{-4}
	20	0.256	9.3×10^{-4}	1.9×10^{-4}	7.5×10^{-5}
	30	0.0759	2.8×10^{-4}	5.7×10^{-5}	2.2×10^{-5}
75	10	11.2	1.7×10^{-1}	4.0×10^{-2}	1.2×10^{-2}
	20	1.40	2.2×10^{-2}	5.0×10^{-3}	1.5×10^{-3}
	30	0.414	6.4×10^{-3}	1.5×10^{-3}	4.6×10^{-4}
100	10	36.7	1.5	4.0×10^{-1}	1.0×10^{-1}
	20	4.58	1.9×10^{-1}	5.0×10^{-2}	1.3×10^{-2}
	30	1.36	5.7×10^{-2}	1.5×10^{-2}	3.7×10^{-3}

TABLE S1. Resonant dipole-dipole and vdW interaction strengths, J and V_{ij} , between pairs of Rydberg states $|r_0\rangle = |nS_{1/2}, m_j = 1/2\rangle$ and $|r_1\rangle = |nP_{3/2}, m_j = 3/2\rangle$ with $n = 50, 75, 100$ for ^{87}Rb at a distance R [1].

	$n = 50$	$n = 75$	$n = 100$
$C_3/2\pi$ (GHz μm ³)	2.05	11.2	36.7
$C_6^{00}/2\pi$ (GHz μm ⁶)	15	1.9×10^3	5.6×10^4
$C_6^{01}/2\pi$ (GHz μm ⁶)	3.1	4.5×10^2	1.5×10^4
$C_6^{11}/2\pi$ (GHz μm ⁶)	1.2	1.4×10^2	3.7×10^3
$\Gamma_0/2\pi$ (kHz)	7.77	2.15	0.88
$\Gamma_1/2\pi$ (kHz)	3.83	1.08	0.44

TABLE S2. Dispersion coefficients of the resonant dipole-dipole and vdW interaction, C_3 and C_6^{ij} , and decay rates Γ_j of Rydberg states $|r_0\rangle = |nS_{1/2}, m_j = 1/2\rangle$ and $|r_1\rangle = |nP_{3/2}, m_j = 3/2\rangle$ with $n = 50, 75, 100$ for ^{87}Rb [1].

are also expressed in terms of their spherical basis components $\vec{d}_\alpha = (d_\alpha^{+1}, d_\alpha^{-1}, d_\alpha^0)$ using the following transformation rules

$$\begin{cases} d_\alpha^x = \frac{d_\alpha^{-1} - d_\alpha^{+1}}{\sqrt{2}} \\ d_\alpha^y = i \frac{d_\alpha^{-1} + d_\alpha^{+1}}{\sqrt{2}} \\ d_\alpha^z = d_\alpha^0 \end{cases} \quad (\text{S3})$$

One can verify that, given the choice of states described in the previous section, the only nonvanishing transition dipole moments are

$$\langle r_0 | d_{-1}^\alpha | r_1 \rangle = \langle r_1 | d_{+1}^\alpha | r_0 \rangle \equiv d, \quad (\text{S4})$$

where, using the notation $|n, L, m_L\rangle$ – with n the principal quantum number, L the orbital angular momentum quantum number, and m_L its projection on the quantization axis z – the relevant Rydberg states are $|r_0\rangle = |n, 0, 0\rangle$ ($nS_{1/2}$ with $m_j = 1/2$) and $|r_1\rangle = |n, 1, 1\rangle$ ($nP_{3/2}$ with $m_j = 3/2$). We also assume that these transition dipole moments are the same for both atoms ($\alpha = A, B$).

From this, one can easily see that the only relevant terms in Eq. (S2) are those responsible for the exchange interaction, i.e., $d_A^{+1}d_B^{-1} + d_A^{-1}d_B^{+1}$. Hence, the transition matrix elements of the resonant exchange dipole–dipole interaction are

$$J(\vec{R}) = \langle r_0 r_1 | V_{dd}(\vec{R}) | r_1 r_0 \rangle = \langle r_1 r_0 | V_{dd}(\vec{R}) | r_0 r_1 \rangle = \frac{d^2}{R^3} \frac{1 - 3 \cos^2 \theta}{2}. \quad (\text{S5})$$

In this work, we consider a quantization axis z aligned with the interatomic direction \vec{R} , thus $\theta = 0$. In this way, we can write

$$J(R) = \frac{C_3}{R^3} \quad (\text{S6})$$

with $C_3 = -d^2 = -|\langle r_0 | d_{-1}^\alpha | r_1 \rangle|^2$ the dispersion coefficient of the dipole–dipole interaction.

van der Waals interactions

At large interatomic separations, the van der Waals (vdW) interaction represents a small perturbative correction to the resonant dipole–dipole coupling J , and decays as $V_{\text{vdW}} = C_6/R^6$, where C_6 is the dispersion coefficient associated with the vdW forces and depends on the specific pair state $|r_i r_j\rangle$ [2]. Within second-order perturbation theory, C_6 can be expressed as [1]

$$C_6^{ij} = \sum_{r', r''} \frac{|\langle r' r'' | V_{dd} | r_i r_j \rangle|^2}{\Delta_{r' r''}^{ij}}, \quad (\text{S7})$$

where V_{dd} is the dipole–dipole interaction operator defined in Eq. (S1), and the sum runs over all intermediate Rydberg states r' and r'' , given a sufficiently small detuning $\Delta_{r' r''}^{ij} = E_{r' r''} - E_{r_i r_j}$, with $E_{r_i r_j}$ the energy of the pair state $|r_i r_j\rangle$. To avoid divergences in the perturbative expression, when evaluating C_6^{01} the symmetric state $|r_1 r_0\rangle$ must be excluded from the sum, as it is resonant with $|r_0 r_1\rangle$ and its contribution is already explicitly accounted for in the resonant exchange interaction. The same consideration applies to the computation of C_6^{10} . Since the vdW dispersion coefficients scale as $C_6 \sim n^{11}$, the ratio between the vdW interaction and the resonant dipole–dipole coupling scales as $V_{\text{vdW}}/J \sim n^7/R^3$. While in the long-distance regime—the primary focus of this work—the vdW contribution becomes less significant, the large principal quantum numbers $n \sim 100$ required to achieve long Rydberg lifetimes make these interactions non-negligible (see Tab. S1).

$\pi J \pi$ protocol

A simple scheme to implement the iSWAP gate with Rydberg atoms – referred to as the $\pi J \pi$ protocol and inspired by molecular platforms [6–10] – consists of three steps:

1. *Toggling π pulses*: The fields Ω_j drive the transitions $|j\rangle \rightarrow |r_j\rangle$ ($j = 0, 1$), transferring the population from the ground-states to the Rydberg states and thereby activating the dipolar interaction. The duration is $T_\pi = \pi/\Omega_{\max}$;
2. *Free dipole-dipole interaction*: By waiting for a time $T_J = \pi/(2J)$, the spin-exchange Hamiltonian H_J generates a maximally entangled state;
3. *De-toggling π pulses*: The fields Ω_j drive the transitions $|r_j\rangle \rightarrow |j\rangle$ ($j = 0, 1$), returning the population from the Rydberg states to the ground-states. The duration is T_π .

The total duration $T_{\pi J \pi}$ of the $\pi J \pi$ sequence is

$$T_{\pi J \pi} \Omega_{\max} = (2T_\pi + T_J) \Omega_{\max} = \pi \left(\frac{4 + \Omega_{\max}/J}{2} \right). \quad (\text{S8})$$

For a reasonable choice of Rabi frequency, e.g., $\Omega_{\max}/2\pi = 1$ MHz, and choosing the principal quantum number $n = 100$ and the interatomic distance $R = 11$ μm – one has $\Omega_{\max}/J = 0.1$, resulting in $T_{\pi J \pi} = 6.4/\Omega_{\max}$, which is approximately 15% faster than the time-optimal gate based on the blockade mechanism [11]. This is promising, but there is a caveat. When $\Omega_{\max} \lesssim J$, the dipolar interaction J significantly affects the dynamics even during the toggling π pulses. Indeed, simulating the $\pi J \pi$ protocol with $\Omega_{\max}/J = 0.1$ reveals that the fidelity F is very low, as shown in Fig. S1(a). Achieving reasonable fidelity requires a much larger ratio Ω_{\max}/J to neglect the effect of dipolar exchange during the toggling pulses – as is the case for molecules. However, increasing this ratio also prolongs the gate duration. For example, for $\Omega_{\max}/J = 50$, the infidelity is $1 - F \approx 10^{-3}$, but the gate duration becomes $T_{\pi J \pi} \Omega_{\max} = 85$, which is excessively long, especially considering the finite lifetimes of Rydberg states, as illustrated in Fig. S1(b), where the effects of spontaneous emission are included in the simulations.

Gate with constant pulses

In the main text, it was shown that the time-optimal U_{iSWAP} gate can be implemented using a pulse with an optimized phase. In this section, we show that the same unitary U_{iSWAP} can also be realized by applying a single global constant pulse of duration T , without any phase modulation – although the resulting gate is considerably slower than the time-optimal one. The duration T is chosen such that, by the end of the pulse, the entire iSWAP operation is completed: the population is transferred to the Rydberg states, the dipolar exchange occurs, and the population returns to the ground states – all within a single step.

In Fig. S1(c), the system is initialized in the state $|01\rangle$, after which constant pulses $\Omega_j(t) = \Omega_{\max}$ ($j = 0, 1$) are applied. The figure shows the time evolution of the population of $|10\rangle$, allowing us to identify when a complete transfer $|01\rangle \rightarrow |10\rangle$ occurs. This is evaluated for different values of the ratio Ω_{\max}/J . A full population transfer is observed, for instance, at $\Omega_{\max}/J = 0.1$ with the “magic” gate time $T\Omega_{\max} = 62.3$, and at $\Omega_{\max}/J = 0.2$ with $T\Omega_{\max} = 31.2$. More generally, the “magic” gate duration T yielding complete transfer scales approximately as the inverse of Ω_{\max}/J , at least for $\Omega_{\max}/J < 1$. For larger ratios, however, the maximum of the transferred population decreases: for example, in Fig. S1(c), the first major peak at $\Omega_{\max}/J = 0.3$ occurs earlier than for $\Omega_{\max}/J = 0.1$, but reaches a smaller maximum and does not achieve unity. To reach lower infidelities and time-optimal performance, it is necessary to optimize the pulse phases.

GRAPE

The GRAPE (Gradient Ascent Pulse Engineering) algorithm is a standard optimal control technique that finds controls $\vec{u}(t)$ minimizing a cost functional $\mathcal{C}[\vec{u}(t)]$ for a Hamiltonian $H(\vec{u}(t))$ [11, 12]. Here, the BFGS method is used [13]. A piecewise-constant ansatz divides the pulse duration T into N steps of length $\Delta t = T/N$ and assuming that within each time-step each control has a constant value, i.e., $\vec{u}(t) = \vec{u}^k$ for $t \in [k\Delta t, (k+1)\Delta t]$ and $k = 0, 1, \dots, N-1$. In the system of two dipole-dipole-interacting atoms driven by two Rydberg excitation fields, the available controls are the Rabi amplitudes $|\Omega_j(t)|$ and phases $\phi_j(t)$ ($j = 0, 1$). We set $|\Omega_0(t)| = |\Omega_1(t)| = \Omega_{\max}$ and $\phi_0(t) = \phi_1(t) = \phi(t)$. This choice simplifies the optimization without affecting the time-optimality of the resulting pulses. Indeed, even when this assumption is relaxed, we find that GRAPE naturally favors equal phases and, at least for relatively small ratios Ω_{\max}/J , drives the Rabi frequencies to their maximum value and keeps them constant throughout the pulse. For large

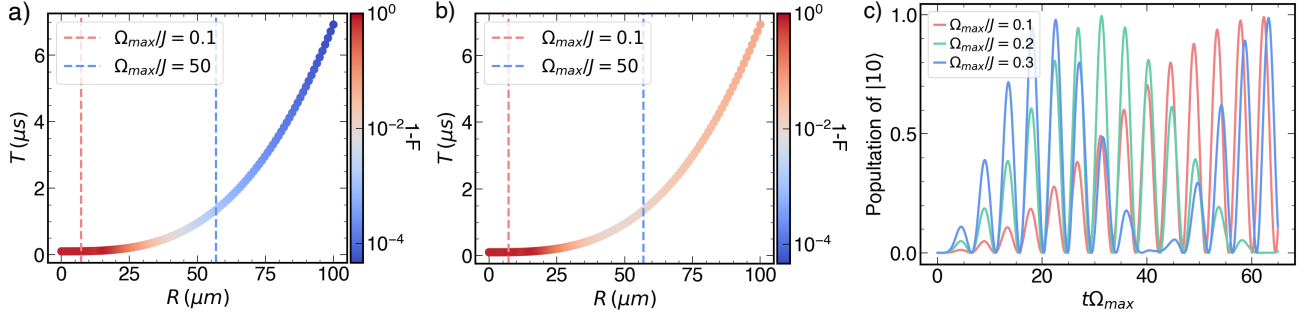


FIG. S1. (a) Simulation of the fidelity $\pi J \pi$ protocol with $\Omega_{\max}/2\pi = 10$ MHz, and $n = 100$, in absence of decay from the Rydberg states. Each point represents a different ratio Ω_{\max}/J , thus a different gate duration T and range R . (b) Same simulation of Fig. S1(a), including also the Rydberg decay, $\Gamma_0/2\pi = 0.88$ kHz and $\Gamma_1/2\pi = 0.44$ kHz. (c) Time evolution of the population of the state $|10\rangle$ when starting from $|01\rangle$ and applying constant global pulses $\Omega_j(t) = \Omega_{\max}$ ($j = 0, 1$) with three different ratios Ω_{\max}/J .

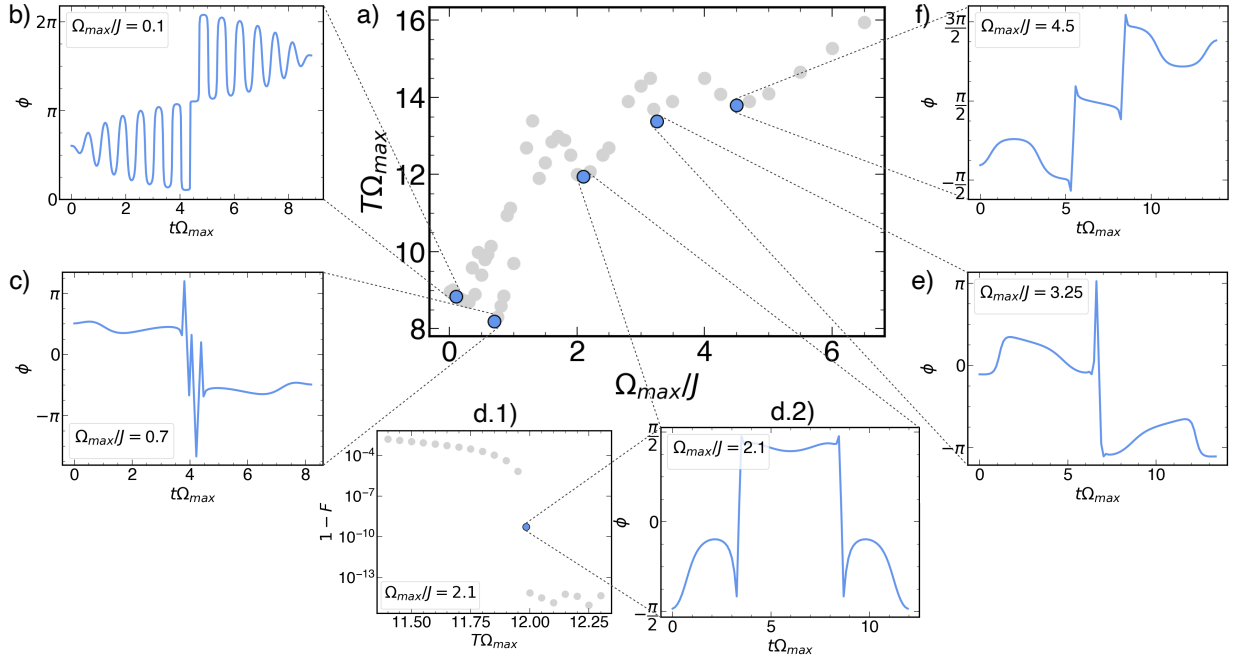


FIG. S2. Time-optimal pulses. (a) The time-optimal gate duration $T\Omega_{\max}$ for different ratios Ω_{\max}/J . (b) Phase $\phi(t)$ of the time-optimal pulse for $\Omega_{\max}/J = 0.1$, with duration $T\Omega_{\max} = 8.84$. (c) Phase $\phi(t)$ of the time-optimal pulse for $\Omega_{\max}/J = 0.7$, with duration $T\Omega_{\max} = 8.2$. (d.1) Infidelity $1 - F$ as a function of the gate time duration $T\Omega_{\max}$ for the ratio $\Omega_{\max}/J = 2.1$. In order to achieve a numerical zero infidelity pulses of duration $T\Omega_{\max} \geq 11.95$ are required. (d.2) Phase $\phi(t)$ of the time-optimal pulse for $\Omega_{\max}/J = 2.1$, with duration $T\Omega_{\max} = 11.95$. (e) Phase $\phi(t)$ of the time-optimal pulse for $\Omega_{\max}/J = 3.25$, with duration $T\Omega_{\max} = 13.38$. (f) Phase $\phi(t)$ of the time-optimal pulse for $\Omega_{\max}/J = 4.5$, with duration $T\Omega_{\max} = 13.8$.

ratios $\Omega_{\max}/J \gtrsim 10$, it is no longer necessary to keep the driving fields on throughout the entire gate, and GRAPE tends to converge to solutions resembling the $\pi J \pi$ protocol, with two laser pulses at the beginning and end of the gate, separated by a period of free dipole–dipole interaction. Three additional parameters, θ , φ , and λ , account for a final global single-qubit rotation $R(\theta, \varphi, \lambda) = \exp(i(\varphi + \lambda)/2)R_z(\varphi)R_y(\theta)R_z(\lambda)$. The full set of optimization parameters thus reads $\vec{u} = \{\phi^k, \theta, \varphi, \lambda\}_{k=0, \dots, N-1}$.

Time-optimal pulses

In Fig. S2, the time-optimal phase profiles $\phi(t)$ obtained with GRAPE for different values of the ratio Ω_{\max}/J are shown. In particular, Fig. S2(a) displays the time-optimal gate duration $T\Omega_{\max}$ as a function of Ω_{\max}/J . The

quantity $T\Omega_{\max}$ represents the minimum pulse duration for which GRAPE identifies a pulse yielding a (numerically) vanishing cost function, i.e., $1 - F \approx 0$ [see Fig. S2(d.1)].

When $\Omega_{\max}/J < 1$, the time-optimal pulses display similar features [see Fig. S2(b)]. In particular, the phase $\phi(t)$ exhibits damped oscillations at frequency J . The Fourier spectra of the pulses show a dominant central peak at the laser resonance frequency, accompanied by additional peaks at frequencies $\pm nJ$ (with odd n). These sidebands, detuned by $\pm nJ$ from resonance, effectively compensate for the energy shifts induced by the dipole–dipole interaction. Moreover, a phase jump of approximately π typically occurs near the middle of the pulse.

When the ratio Ω_{\max}/J approaches or exceeds unity, the behavior of the phase $\phi(t)$ becomes less regular, although the characteristic phase jump near the middle of the pulse generally persists [see Figs. S2(c)–(f)].

The shortest pulse is obtained for $\Omega_{\max}/J = 0.7$, with $T\Omega_{\max} = 8.2$ [see Fig. S2(c)]. Relatively short durations are also found for $\Omega_{\max}/J = 2.1$ ($T\Omega_{\max} = 11.95$), $\Omega_{\max}/J = 3.25$ ($T\Omega_{\max} = 13.38$), and $\Omega_{\max}/J = 4.5$ ($T\Omega_{\max} = 13.8$) [see Figs. S2(d.2)–(f)].

Simulation of motion

To obtain realistic estimates of the fidelity of the optimal pulses, it is necessary to include the motional degrees of freedom of the atoms. These can affect the dipole–dipole interaction by altering the interatomic distance, or induce decoherence by generating entanglement between internal and motional states. In this section, we discuss the kinetic Hamiltonian, the effects of atomic displacements on the interaction strength, and the impact of photon recoil. For each contribution, we estimate its effect on the pulse infidelity through numerical simulations and analytical calculations of the corresponding coupling strengths.

Kinetic energy

The three-dimensional potential of the optical tweezers in which the atoms are trapped – prior to the Rydberg excitation pulses – can be modeled as three harmonic oscillators with angular frequencies ω_ℓ , where $\ell = x$ (axial direction) and $\ell = y, z$ (radial directions) [see Fig. S3(d)]. Typically, $5\omega_x \approx \omega_y \approx \omega_z$. The kinetic Hamiltonian of the atoms, H_K , is given by

$$H_K = - \sum_{\alpha=A,B} \frac{\vec{p}_\alpha^2}{2m}, \quad (S9)$$

where $\vec{p}_\alpha = (p_\alpha^x, p_\alpha^y, p_\alpha^z)$, and $p_\alpha^\ell = \sqrt{m\omega_\ell/2}(a_{\ell,\alpha}^\dagger - a_{\ell,\alpha})$ is the momentum operator of atom α along direction $\ell = x, y, z$. Here, $a_{\ell,\alpha}$ and $a_{\ell,\alpha}^\dagger$ are the corresponding ladder operators. We omit the trapping potential, as optical tweezers are typically turned off during the Rydberg excitation pulses.

Distance fluctuations

Equation (S5) describes the behavior of the exchange dipole-dipole interaction strength J as a function of the vector distance \vec{R} between two atoms. Namely, it depends on the magnitude of the distance R and the polar angle θ between the vector \vec{R} and the quantization axis z . In the following, we analyze how the atomic motion affects the interatomic distance R , the angle θ , and consequently the coupling strength J .

Variations of the radius R

The position operator of molecule α with respect to the center of its optical trap – i.e., the minimum of the three trapping potentials – is $\vec{r}_\alpha = (x_\alpha, y_\alpha, z_\alpha)$, where $r_{\ell,\alpha} = \sqrt{1/(2m\omega_\ell)}(a_{\ell,\alpha} + a_{\ell,\alpha}^\dagger)$ and $\ell = x, y, z$.

Consider the reference frame in which x is the axial axis of the tweezers, and the interatomic separation vector \vec{R} lies along the z axis: $\vec{R} = (0, 0, R)$ [see Fig. S3(d)].

In the presence of motion – and even at zero temperature, due to the finite width of the motional ground-state wave function – computing the distance between atoms requires accounting for the position fluctuations \vec{r}_α . The perturbed

intermolecular separation vector thus reads $\vec{R}' = \vec{R} + \vec{r}_A - \vec{r}_B$. For sufficiently strong trapping potentials ω_ℓ and sufficiently low temperature T_{temp} , the relative dimensionless deviations $\epsilon_\ell = (r_{\ell,A} - r_{\ell,B})/R$ are small and can be treated as perturbative parameters. Hence, the magnitude of the perturbed distance is

$$R' = R \sqrt{\epsilon_x^2 + \epsilon_y^2 + (1 + \epsilon_z)^2} = R \sqrt{1 + \epsilon}, \quad (\text{S10})$$

where ϵ is the collective perturbative parameter that takes into account the motion in all directions, its explicit expression is

$$\epsilon = 2\epsilon_z + \epsilon_x^2 + \epsilon_y^2 + \epsilon_z^2. \quad (\text{S11})$$

The dipole-dipole perturbed interaction strength J' depends on the inverse of the cubic of R' (see Eq. (S5)), then we can expand it up to second order in ϵ

$$\frac{1}{R'^3} = \frac{1}{R^3} \left(1 - \frac{3}{2}\epsilon + \frac{15}{8}\epsilon^2 + o(\epsilon^3) \right). \quad (\text{S12})$$

Variations of the angle θ

Given the reference frame in which x is the axis of the tweezers and the intermolecular separation vector \vec{R} lies along the z axis [see Fig. S3(d)], the angle θ in Eq. (S5) is zero, $\theta = 0$. Once the perturbations \vec{r}_j are introduced, the perturbed angle θ' is no longer zero. The angular deviation θ' can be computed by projecting the vector \vec{R}' onto the z axis (unit vector \hat{z}), thus

$$\cos \theta' = \frac{\vec{R}' \cdot \hat{z}}{R'} = \frac{1 + \epsilon_z}{\sqrt{1 + \epsilon}}. \quad (\text{S13})$$

The angular part of the perturbed coupling strength J' in Eq. (S5) becomes

$$\frac{1 - 3 \cos^2 \theta'}{2} = \frac{1}{2} \left(1 - 3 \frac{(1 + \epsilon_z)^2}{1 + \epsilon} \right) = -1 + \frac{3}{2} (\epsilon_x^2 + \epsilon_y^2) + o(\epsilon^3). \quad (\text{S14})$$

Variations of the coupling strength

Combining the effects of motion on both the intermolecular distance R and the angle θ , Eqs. (S12) and (S14), one can estimate the perturbed coupling constant J' as

$$J' = \frac{d^2}{R'^3} \frac{1 - 3 \cos^2 \theta'}{2} = J \left(1 - 3\epsilon_z + 3(2\epsilon_z^2 - \epsilon_x^2 - \epsilon_y^2) \right) + o(\epsilon^3), \quad (\text{S15})$$

where, in the last line, we used the fact that in this frame $J = -d^2/R^3$. Therefore, the exchange interaction Hamiltonian H'_J , accounting for the effect of atomic motion, becomes

$$H'_J = J \left[1 - 3 \frac{z_A - z_B}{R} + 6 \frac{(z_A - z_B)^2}{R^2} - 3 \frac{(x_A - x_B)^2}{R^2} - 3 \frac{(y_A - y_B)^2}{R^2} + \dots \right] (|r_0 r_1\rangle \langle r_1 r_0| + \text{h.c.}) \quad (\text{S16})$$

$$= H_J + H_J^{(1,z)} + H_J^{(2,z)} + H_J^{(2,x)} + H_J^{(2,y)} + \dots \quad (\text{S17})$$

where $H_J^{(n,\ell)}$ refers to the motion-noise-term at the perturbative order n relative to the direction $\ell = x, y, z$.

Similarly, for the van der Waals interactions $V_{\text{vdW}} \sim R^{-6}$, one can demonstrate that the Hamiltonian in the presence of distance fluctuations at first-order reads

$$H'_{\text{vdW}} = H_{\text{vdW}} + H_{\text{vdW}}^{(1,z)} \quad (\text{S18})$$

$$= \sum_{i,j} V_{ij} \left[1 - 6 \frac{z_A - z_B}{R} \right] |r_i r_j\rangle \langle r_i r_j| \quad (\text{S19})$$

where H_{vdW} is the interaction Hamiltonian in absence of distance fluctuations and $H_{\text{vdW}}^{(1,z)}$ refers to the motion-noise-term at the first perturbative order relative to the direction $\ell = z$. Higher-order terms are not required, as even the first-order term does not significantly affect the dynamics (see Tab. S3).

Photon recoil

When an atom absorbs a photon, it also acquires the corresponding momentum $k = 2\pi/\lambda$, where λ is the wavelength of the incident light. This momentum kick perturbs the motional state of the atom and can be modeled by introducing the Lamb–Dicke parameter $\eta_j = 2\pi\sqrt{1/(2m\omega_{\bar{\ell}})}/\lambda_j$, where $\bar{\ell}$ denotes the propagation direction of the laser field Ω_j ($j = 0, 1$). With this correction, the driven-field Hamiltonian H_Ω becomes

$$H'_\Omega = \sum_{j,\alpha} \frac{\Omega_j}{2} \left(e^{i\phi_j + i\eta_j(a_{\bar{\ell},\alpha} + a_{\bar{\ell},\alpha}^\dagger)} |j\rangle \langle r_j|_\alpha + \text{h.c.} \right). \quad (\text{S20})$$

For simplicity, in the expression of η_j we use the wavelength λ_j of the single-photon transition $|j\rangle \leftrightarrow |r_j\rangle$ (even if forbidden), which corresponds to a worst-case estimate; in practice, η_j is significantly smaller when the Rydberg excitation involves a two- or three-photon transition.

Unitary transformation

To better illustrate the effects of the momentum kick, it is useful to perform the following unitary transformation

$$U = \exp \left[- \sum_{\alpha,j} i\eta_j(a_{\bar{\ell},\alpha} + a_{\bar{\ell},\alpha}^\dagger) |r_j\rangle \langle r_j|_\alpha \right]. \quad (\text{S21})$$

It is straightforward to verify that the following transformation rules hold

$$U^\dagger a_{\bar{\ell},\alpha} U = a_{\bar{\ell},\alpha} + i \sum_{j=0,1} \eta_j |r_j\rangle \langle r_j|_\alpha, \quad (\text{S22})$$

$$U^\dagger |j\rangle \langle r_j|_\alpha U = \exp[-i\eta_j(a_{\bar{\ell},\alpha} + a_{\bar{\ell},\alpha}^\dagger)] |j\rangle \langle r_j|_\alpha, \quad (\text{S23})$$

$$U^\dagger |r_j\rangle \langle r_i|_\alpha U = \exp[i(\eta_j - \eta_i)(a_{\bar{\ell},\alpha} + a_{\bar{\ell},\alpha}^\dagger)] |r_j\rangle \langle r_i|_\alpha. \quad (\text{S24})$$

Therefore, the kinetic, driving-laser-field, dipole–dipole interaction, and decay Hamiltonians transform, respectively, as

$$U^\dagger H_K U = H_K + \frac{2\pi^2}{m\lambda^2} \sum_\alpha \mathbb{P}_\alpha^r + \frac{2\pi}{m\lambda} \sum_\alpha \mathbb{P}_\alpha^r p_\alpha^{\bar{\ell}}, \quad (\text{S25})$$

$$U^\dagger H'_\Omega U = \sum_{j,\alpha} \frac{\Omega_j}{2} (e^{i\phi_j} |j\rangle \langle r_j|_\alpha + \text{h.c.}) = H_\Omega, \quad (\text{S26})$$

$$U^\dagger H'_J U = H'_J, \quad (\text{S27})$$

$$U^\dagger H_\Gamma U = H_\Gamma, \quad (\text{S28})$$

where it is assumed that $\eta_0 = \eta_1$, a good approximation, e.g., for $n = 100$ we have $|\eta_0 - \eta_1| \approx 10^{-6}$; here, $p_\alpha^{\bar{\ell}}$ denotes the momentum operator along the direction $\bar{\ell}$ of atom α , and \mathbb{P}_α^r denotes the projector onto the Rydberg-state manifold of atom α

$$\mathbb{P}_\alpha^r = \sum_{j=0,1} |r_j\rangle \langle r_j|_\alpha. \quad (\text{S29})$$

Therefore, the only difference with respect to the unperturbed Hamiltonian is the presence of the two terms in Eq. (S25), which encapsulate the twofold effect of photon recoil. The first term corresponds to a constant detuning of magnitude $2\pi^2/(m\lambda^2)$ on the Rydberg states and will be referred to as H_K^{detuning} , representing the kinetic energy imparted by a photon of the laser field with wavelength λ . The second term represents a coupling between the motional degrees of freedom along the $\bar{\ell}$ direction and the internal states, and will be referred to as H_K^{coupling} . This operator thus generates entanglement between the internal and motional states, resulting in decoherence of the former.

Relevant terms

Summarizing the results above, the total Hamiltonian H' , once corrected for the effects of distance fluctuations H'_J in Eq. (S17) and photon recoil, H_K^{detuning} and H_K^{coupling} in Eq. (S25), and including the vdW interactions H_{vdW} as well as the Rydberg decay non-Hermitian term H_Γ , becomes

$$H' = H + H_{\text{vdW}} + H_J^{(1,z)} + H_J^{(1,z)} + H_J^{(2,z)} + H_J^{(2,x)} + H_J^{(2,y)} + H_K^{\text{detuning}} + H_K^{\text{coupling}} + H_\Gamma, \quad (\text{S30})$$

where H is the unperturbed Hamiltonian, $H = H_\Omega + H_J + H_K$ (Eq. 1 in the main text). It is possible to estimate which of the nine noisy terms discussed above is most relevant, both numerically and analytically. In particular, in Tab. S3, the coupling strength of each term is computed analytically, while the pulse infidelity is numerically simulated in the presence of only that term. This analysis is performed for both time-optimal and vdW-robust pulses. For the analytical estimation of the strength of each noisy term, the approach of Ref. [14] is followed. The terms $H_J^{(1,z)}$ and H_K^{coupling} in Eq. (S30) are not resonant, i.e., the operators acting on the motional Hilbert space do not preserve the number of excitations, since the ladder operators are applied only once. In contrast quadratic terms such as $H_J^{(2,z)}$ contain combinations of ladder operators of the form $a_{z,A}a_{z,B}^\dagger$ that preserve the total energy. However, given that the motional detuning $\omega_z/2\pi = 100$ kHz is small compared to the interaction energy scale $J/2\pi \approx 1\text{--}10$ MHz, the off-resonant terms can be treated analogously to the resonant ones. For example, the magnitude of the first-order term in the distance fluctuations, $H_J^{(1,z)}$, can be evaluated as

$$\frac{\Delta E_J^{(1,z)}}{J} = \frac{3\sigma_{z_A-z_B}}{R} = \frac{3}{R} \sqrt{\frac{1}{2m\omega_z} \coth\left(\frac{\omega_z}{2k_B T_{\text{temp}}}\right)}, \quad (\text{S31})$$

with $\sigma_{z_A-z_B}$ the standard deviation of the displacement operator $z_A - z_B$, evaluated over a thermal distribution of the states. Similarly, the magnitude of the other motion-related terms are

$$\frac{\Delta E_J^{(2,z)}}{J} = \frac{6\sigma_{(z_A-z_B)^2}}{R^2} = \frac{6\sqrt{2}}{m\omega_z R} \coth\left(\frac{\omega_z}{2k_B T_{\text{temp}}}\right), \quad (\text{S32})$$

$$\frac{\Delta E_J^{(2,x)}}{J} = \frac{3\sigma_{(x_A-x_B)^2}}{R^2} = \frac{3\sqrt{2}}{m\omega_x R} \coth\left(\frac{\omega_x}{2k_B T_{\text{temp}}}\right), \quad (\text{S33})$$

$$\frac{\Delta E_J^{(2,y)}}{J} = \frac{3\sigma_{(y_A-y_B)^2}}{R^2} = \frac{3\sqrt{2}}{m\omega_y R} \coth\left(\frac{\omega_y}{2k_B T_{\text{temp}}}\right), \quad (\text{S34})$$

$$\frac{\Delta E_{\text{vdW}}^{(1,z)}}{V_{\text{vdW}}} = \frac{6\sigma_{z_A-z_B}}{R} = \frac{6}{R} \sqrt{\frac{1}{2m\omega_z} \coth\left(\frac{\omega_z}{2k_B T_{\text{temp}}}\right)}, \quad (\text{S35})$$

where $\sigma_{(z_A-z_B)^2} = \sqrt{2}\sigma_{z_A-z_B}^2$ is the standard deviation of the squared of the displacement operator $(z_A - z_B)^2$. The magnitude of the motion-internal space coupling emerging from photon recoil, H_K^{coupling} , can be similarly evaluated as

$$\frac{\Delta E_K^{\text{coupling}}}{2\pi} = \frac{1}{\lambda} \sqrt{\frac{\omega_\ell}{m} \coth\left(\frac{\omega_\ell}{2k_B T_{\text{temp}}}\right)}. \quad (\text{S36})$$

Table S3 shows, consistently with both the analytical estimates of the coupling strengths and the numerical fidelity calculations, that the main source of error affecting the time-optimal pulses arises from the vdW interactions. Once these forces are included in the optimization and vdW-robust pulses are obtained, the dominant error sources become, in decreasing order, the Rydberg decay H_Γ , the first-order atomic displacement along the interatomic z direction $H_J^{(1,z)}$, and the photon-recoil coupling term H_K^{coupling} . Note that the coupling term associated with spontaneous emission, reported in Tab. S3 as the decay rate Γ , is smaller than the others; however, it represents the magnitude of a non-Hermitian contribution to the Hamiltonian and is therefore not directly comparable to the other (Hermitian) noise terms.

Recapture probability

Once the excitation pulse is applied and the optical tweezers are turned back on, the scheme is expected to ensure a high recapture probability of the atoms [4, 15]. The dipolar force exerted by one atom on the other is given by

Noise term		1 - F		Coupling strength ($2\pi \times \text{Hz}$)
		Time-optimal	vdW-robust	
No noise	\emptyset	7.0×10^{-6}	-	0
vdW interactions	H_V	1.3×10^{-2}	2.0×10^{-4}	9.6×10^5
Rydberg decay	H_Γ	7.0×10^{-4}	7.0×10^{-4}	1.3×10^3
1st order motion along z (J term)	$H_J^{(1,z)}$	4.3×10^{-5}	3.7×10^{-4}	2.4×10^4
2nd order motion along x	$H_J^{(2,x)}$	$< 10^{-7}$	$< 10^{-7}$	6.6×10^2
2nd order motion along y	$H_J^{(2,y)}$	$< 10^{-7}$	$< 10^{-7}$	5.9×10
2nd order motion along z	$H_J^{(2,z)}$	$< 10^{-7}$	$< 10^{-7}$	1.2×10^2
1st order motion along z (V_{vdW} term)	$H_{\text{vdW}}^{(1,z)}$	$< 10^{-7}$	$< 10^{-7}$	9.2×10^3
Photon recoil H_K^{detuning} with	$\Delta_j = 0$	1.3×10^{-5}	8.7×10^{-6}	2.6×10^4
	$\Delta_j = 2\pi^2/m\lambda^2$	$< 10^{-7}$	$< 10^{-7}$	
Photon recoil H_K^{coupling} with	$\bar{\ell} = x$	2.3×10^{-5}	1.9×10^{-5}	7.3×10^4
	$\bar{\ell} = z$	4.9×10^{-5}	5.1×10^{-5}	4.9×10^4
All	$\bar{\ell} = z$	1.3×10^{-2}	9.9×10^{-4}	-

TABLE S3. To compute these terms, the following parameters were adopted: a pulse with $\Omega_{\text{max}}/J = 2.1$, temperature $T_{\text{temp}} = 1 \mu\text{K}$, maximum Rabi frequency $\Omega_{\text{max}}/2\pi = 10 \text{ MHz}$, trapping frequencies $\omega_z/2\pi = 100 \text{ kHz} = 5\omega_x/2\pi$, and Rydberg states with principal quantum number $n = 100$. The value $1 - F = 7.0 \times 10^{-6}$ (first line) represents the numerical zero at which GRAPE optimization is stopped for the time-optimal pulse. For the vdW-robust pulse, the optimization is halted at $1 - F = 2.0 \times 10^{-4}$ to avoid an excessive gate duration and increased decay errors. The coupling strengths are computed from the prefactors in the analytical expression of the Hamiltonian H' , with $\hbar = 1$.

$F = |\partial J/\partial R| = 3C_3/R^4$, corresponding to an acceleration $a = 3C_3/(mR^4)$ on each atom. Since the interatomic distance R is large compared to the scale of atomic motion, the acceleration can be considered constant during the pulse sequence. The resulting displacement of an atom during the pulse can thus be estimated as

$$\Delta z = \frac{1}{2}aT^2 = \frac{3}{2} \frac{C_3 T^2}{mR^4} \approx 0.06 \text{ nm}, \quad (\text{S37})$$

using the parameters $n = 100$, $T = 190 \text{ ns}$, $R = 19.7 \mu\text{m}$, and $m = 1.4 \times 10^{-25} \text{ kg}$ (vdW-robust pulse for $\Omega_{\text{max}}/J = 2.1$). This displacement is several orders of magnitude smaller than the characteristic harmonic oscillator length, $z_{\text{osc}} = \sqrt{1/(2m\omega_z)} \approx 24 \text{ nm}$ for $\omega_z/2\pi = 100 \text{ kHz}$, and therefore the recapture of the atoms should be straightforward.

Gate fidelity with mixed states

In the cost functional employed by GRAPE to optimize both the time-optimal and vdW-robust pulses implementing the iSWAP gate, the Bell-state fidelity F is used as the figure of merit

$$F = \frac{1}{16} \left| \sum_q \langle \psi_q | R^{\otimes 2} U_{\text{iSWAP}} | q \rangle \right|^2, \quad (\text{S38})$$

where $|\psi_q\rangle$ is the actual two-qubit final state obtained by applying the pulse to $|q\rangle$, from the computational basis $|q\rangle \in \{|00\rangle, |01\rangle, |10\rangle, |11\rangle\}$. $|\psi_q\rangle$ is therefore compared to the target state $U_{\text{iSWAP}}|q\rangle$ up to a final global single-qubit operation $R(\theta, \varphi, \lambda) = e^{i(\varphi+\lambda)/2} R_z(\varphi) R_y(\theta) R_z(\lambda)$, where φ , θ , and λ are rotation angles treated as additional optimization parameters. The expression in Eq. (S38) is convenient because it guarantees not only the correct population transfer among the computational basis states but also the preservation of coherence, i.e., the relative phases between them. However, this form cannot be directly applied to evaluate the fidelity of the pulses in the presence of atomic motion. When coupling to the motional degrees of freedom is included, the final internal state generally becomes entangled with the motional state and is thus described by a mixed density matrix rather than a pure state. Furthermore, the fidelity then depends on the initial motional state, requiring an average over all possible

initial conditions. To properly account for these effects, we adopt the following fidelity function

$$F' = \sum_{m=0}^M \frac{b_m}{\dim Q^2} \left| \sum_q \sqrt{\mathcal{F}(\rho_{qm}, \rho_q^{\text{targ}})} e^{i\phi_{qm}} \right|^2. \quad (\text{S39})$$

The first sum in Eq. (S39) runs over all harmonic oscillator eigenstates $|m\rangle$ with eigenenergy E_m , where $b_m = \exp(-E_m/k_B T_{\text{temp}})/\mathcal{Z}$ is the corresponding Boltzmann factor at temperature T_{temp} , k_B is the Boltzmann constant, and $\mathcal{Z} = \sum_{m=0}^M \exp(-E_m/k_B T_{\text{temp}})$ is the partition function. Accordingly, we assume a thermal distribution of the initial motional excitations. The cutoff M must be chosen sufficiently large to ensure an accurate description of the system. The second sum runs over all computational basis states $|q\rangle$. The final reduced density matrix ρ_{qm} is obtained by evolving the pure product state $|q, m\rangle$ under the gate unitary $U(T, 0)$ and tracing out the motional degrees of freedom, $\rho_{qm} = \text{Tr}_{\text{mot}}\{U(T, 0)|q, m\rangle\langle q, m|U(T, 0)^\dagger\}$. The target density matrix ρ_q^{targ} is instead obtained by applying the ideal gate U_{iSWAP} to the internal state $|q\rangle$ in the absence of motion and other noise sources. Finally, $\mathcal{F}(\rho, \sigma)$ denotes the Uhlmann fidelity, which quantifies the overlap between two density matrices [16, 44].

$$\mathcal{F}(\rho, \sigma) = \left(\text{Tr} \sqrt{\sqrt{\rho}\sigma\sqrt{\rho}} \right)^2. \quad (\text{S40})$$

The Uhlmann fidelity is a real quantity that quantifies the overlap between the target pure state ρ_q^{targ} and the actual reduced density matrix ρ_{qm} [18]. However, it does not account for the coherence between different computational basis states q . To incorporate this information, we multiply the Uhlmann fidelity by the accumulated phase $\phi_{qm} = \arg(\langle \psi_q^{\text{targ}} | \psi_{qm} \rangle)$, where $|\psi_{qm}\rangle$ denotes the actual final state (including both internal and motional degrees of freedom) evolved from the initial state $|q, m\rangle$, and $|\psi_q^{\text{targ}}\rangle = U_{\text{iSWAP}}|q\rangle$ represents the ideal target state for $|q\rangle$, formally tensored with a uniform superposition (all-ones vector) in the motional subspace.

The fidelity function in Eq. (S39) ensures that, for every motional state $m < M$ and every internal state q in the computational basis, the pulse drives the system to the target state $|\psi_q^{\text{targ}}\rangle$ up to a phase factor ϕ_{qm} , which must be identical for all q in order to preserve coherence.

Performance with noise

In this section, the performance of the time-optimal and vdW-robust pulses is evaluated in the presence of different error sources, namely the finite lifetime of the Rydberg states, the coupling to motional degrees of freedom, and the residual off-resonant vdW interactions. All results are summarized in Fig. S3.

Performance with spontaneous emission

In Figs. S2(b)-(c), the fidelity of the time-optimal pulses is analyzed, including the decay term H_Γ . One can observe that, for a fixed interatomic distance R , larger Rabi frequencies Ω_{max} lead to higher fidelities, as they make the pulses faster and reduce the time spent in the Rydberg states. The same trend holds for shorter distances R , since the interaction strength $J \sim R^{-3}$ implies that the gate duration T is generally shorter for small R , resulting in less time spent in the Rydberg states and reduced susceptibility to decay. There are some values of the ratio Ω_{max}/J – thus of the distance R – for which the duration T is particularly short with respect to the nearby pulses, e.g., $T\Omega_{\text{max}} = 0.7$ [see Fig. S2(c)] and $T\Omega_{\text{max}} = 2.1$ [see Fig. S2(d.2)], therefore these points realize particularly good pulses. For example, for $\Omega_{\text{max}}/J = 2.1$, the time spent in Rydberg states is $T_{\text{Ryd}}\Omega_{\text{max}} = 10.6$, and choosing $\Omega_{\text{max}} = 10$ MHz results in an infidelity $1 - F = 7.0 \times 10^{-4}$.

Performance with motion

In Figs. S3(e)–(f), the fidelity of the optimal pulses is analyzed, taking into account both the finite lifetime of the Rydberg states and the atomic motion along the radial z direction (including distance fluctuations and photon recoil). As discussed above, for a fixed interatomic distance R , increasing the maximum Rabi frequency Ω_{max} generally improves the fidelity, as the gate becomes faster. However, in contrast to the case where only decay is considered, for a fixed Rabi frequency Ω_{max} , the shortest pulses are not necessarily those with the highest fidelity [see Fig. S2(f)].

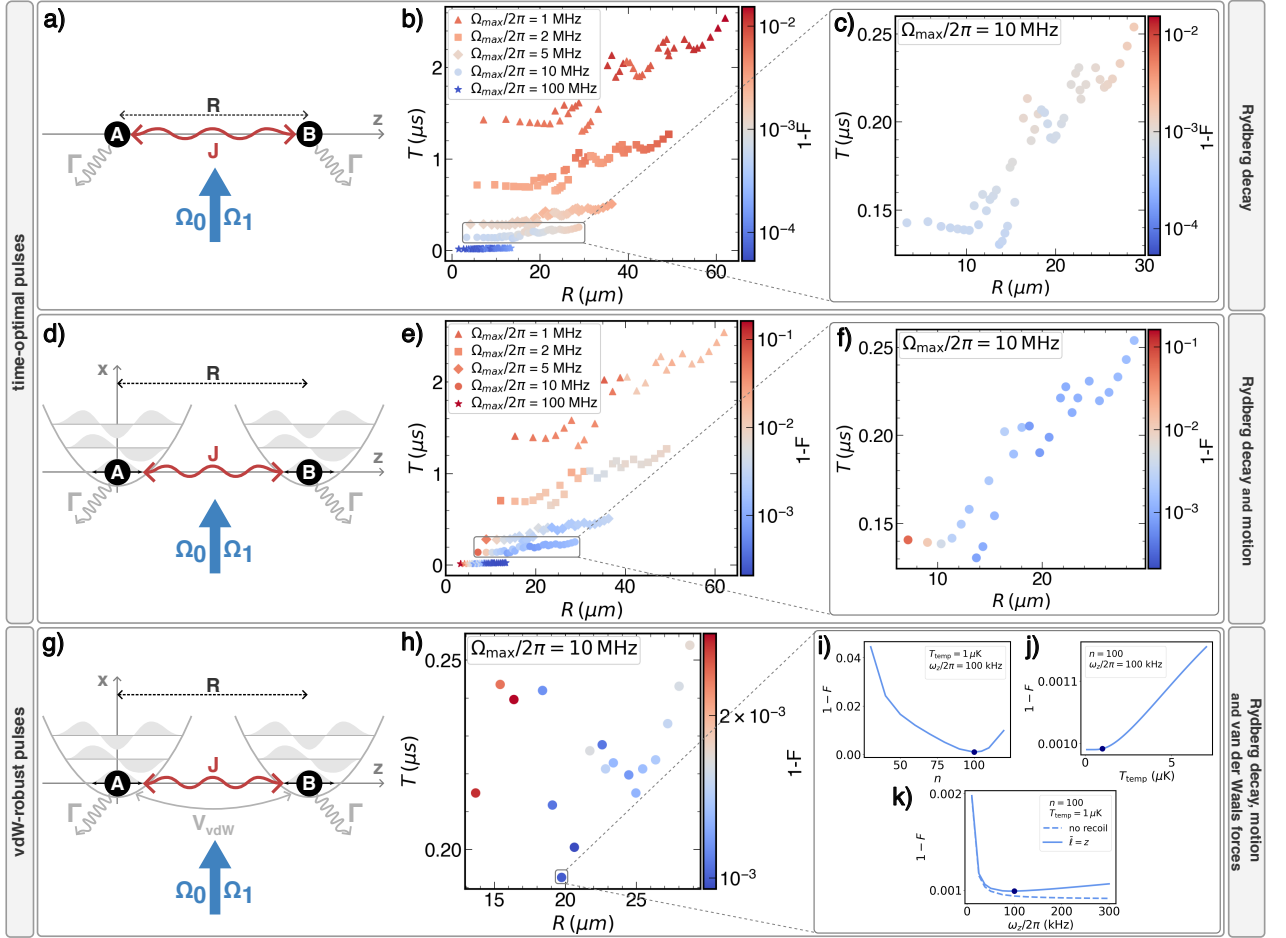


FIG. S3. (a) Schematic representation of the two interacting atoms at a distance R , with global external driving fields Ω_j ($j = 0, 1$), and with decay rate Γ_j . (b) Fidelity of the time-optimal pulses [see Fig. S2] in the presence of spontaneous emission, with $n = 100$ and different Rabi frequencies Ω_{\max} . The time duration T and the range R of each pulse depends on the ratio Ω_{\max}/J and the maximum Rabi frequency Ω_{\max} . (c) Zoom-in on the data points for $\Omega_{\max}/2\pi = 10$ MHz. (d) Schematic representation of the two interacting atoms at a distance R , with global external driving fields Ω_j ($j = 0, 1$), with decay rate Γ_j and moving inside the radial harmonic-like trapping potential of the tweezers. (e) Fidelity of the time-optimal pulses [see Fig. S2] in the presence of spontaneous emission and radial motion, with $n = 100$ and different Rabi frequencies Ω_{\max} . The time duration T and the range R of each pulse depends on the ratio Ω_{\max}/J and the maximum Rabi frequency Ω_{\max} . (f) Zoom-in on the data points for $\Omega_{\max}/2\pi = 10$ MHz. (g) Schematic representation of the two interacting atoms at a distance R , with global external driving fields Ω_j ($j = 0, 1$), with decay rate Γ_j , moving inside the radial harmonic-like trapping potential of the tweezers, and with van der Waals interactions V_{vdW} . (h) Fidelity of the vdW-robust pulses in the presence of spontaneous emission, radial motion and vdW interactions, with $n = 100$ and $\Omega_{\max}/2\pi = 10$ MHz. The time duration T and the range R of each pulse depends on the ratio Ω_{\max}/J and the maximum Rabi frequency Ω_{\max} . (i) Fidelity F of the time-optimal pulse for $\Omega_{\max}/J = 2.1$ as a function of the principal quantum number n . (j) Fidelity F of the time-optimal pulse for $\Omega_{\max}/J = 2.1$ as a function of the temperature T_{temp} . (k) Fidelity F of the time-optimal pulse for $\Omega_{\max}/J = 2.1$ as a function of the radial trapping frequency $\omega_z/2\pi$. The solid line corresponds to the case where the momentum kick occurs along the interatomic direction ($\bar{\ell} = z$). The dashed line corresponds to the case where there is no photon recoil

This occurs because, at short distances, the effect of atomic motion is much stronger and dominates over spontaneous emission—indeed, Eq. (S31) shows that the former scales as $1/R$. Conversely, for very long-range gates, where the effects of atomic motion are no longer significant, the fidelity decreases due to the finite lifetime of the Rydberg states and the longer pulse durations. Optimal performance is therefore achieved at intermediate distances. For example, the pulse with $\Omega_{\max}/J = 2.1$ [see Fig. S2(d.2)] achieves an infidelity of $1 - F = 7.8 \times 10^{-4}$ for $\Omega_{\max}/2\pi = 10$ MHz, with $T_{\text{temp}} = 1 \mu\text{K}$.

Performance with van der Waals interactions

Through numerical simulations, we verified that the vdW interactions do not significantly affect the population dynamics during the time-optimal pulses, but they lead to the accumulation of an unwanted phase, particularly on the qubit state $|00\rangle$, since V_{00} is the largest vdW interaction strength (see Tab. S1). The time-optimal pulse with $\Omega_{\max}/J = 2.1$, using $n = 100$ and $\Omega_{\max}/2\pi = 10$ MHz, and including the vdW interactions H'_{vdW} , yields an infidelity of $1 - F = 1.3 \times 10^{-2}$ – an order of magnitude larger than in the case with only decay and motion. This infidelity can be reduced in two ways: (i) Keep the same pulses shown in Fig. S2 and determine the optimal principal quantum number n that maximizes F , balancing longer Rydberg lifetimes (for large n) against weaker vdW interactions (for small n). For example, for the time-optimal pulse with $\Omega_{\max}/J = 2.1$, the optimal principal quantum number is $n \approx 70$, with an infidelity $1 - F = 3.4 \times 10^{-3}$, but also a reduced range. (ii) Fix the highest achievable principal quantum number (to minimize decay errors), e.g., $n = 100$, and find new pulses that are inherently robust to vdW interactions by including the vdW Hamiltonian H_{vdW} directly in the GRAPE optimization. The time-optimal pulses are used as initial guesses, and, if necessary, their duration T can be slightly increased to adapt to the presence of vdW interactions [19]. For each value of Ω_{\max}/J , there exists a different vdW-robust pulse corresponding to each ratio Ω_{\max}/V_{00} ; thus, the robust pulses also depend explicitly on the value of Ω_{\max} . This second strategy consistently produces higher fidelities, and we therefore adopt it. In general, for small ratios $\Omega_{\max}/J < 1$, GRAPE fails to find robust pulses with durations comparable to the time-optimal ones [see Fig. S3(h)]. This is because small Ω_{\max}/J also implies small R , which enhances the effect of vdW interactions. Conversely, for large ratios $\Omega_{\max}/J \gtrsim 3$, GRAPE can reduce the sensitivity to vdW interactions while keeping the same pulse duration. Intermediate ratios Ω_{\max}/J yield robust pulses at the cost of slightly longer durations. In Fig. S3(h), the performance of a group of vdW-robust pulses for different values of the ratio Ω_{\max}/J is analyzed. In Figs. S3(e)–(g), the fidelity of the robust pulse $\Omega_{\max}/J = 2.1$ is analyzed as a function of the principal quantum number n , the temperature T_{temp} and the radial trapping frequency ω_z .

* bergonzoni@unistra.fr

† pupillo@unistra.fr

- [1] N. Šibalić, J. Pritchard, C. Adams, and K. Weatherill, Arc: An open-source library for calculating properties of alkali rydberg atoms, *Computer Physics Communications* **220**, 319 (2017).
- [2] M. Saffman, T. G. Walker, and K. Mølmer, Quantum information with rydberg atoms, *Rev. Mod. Phys.* **82**, 2313 (2010).
- [3] L. Chomaz, I. Ferrier-Barbut, F. Ferlaino, B. Laburthe-Tolra, B. L. Lev, and T. Pfau, Dipolar physics: a review of experiments with magnetic quantum gases, *Reports on Progress in Physics* **86**, 026401 (2022).
- [4] G. Emperauger, M. Qiao, G. Bernet, C. Chen, R. Martin, Y. T. Chew, B. Gély, L. Klein, D. Barredo, A. Browaeys, and T. Lahaye, Benchmarking direct and indirect dipolar spin-exchange interactions between two rydberg atoms, *Physical Review A* **111**, 10.1103/physreva.111.062806 (2025).
- [5] M. L. Wall, K. Maeda, and L. D. Carr, Realizing unconventional quantum magnetism with symmetric top molecules, *New Journal of Physics* **17**, 025001 (2015).
- [6] K.-K. Ni, T. Rosenband, and D. D. Grimes, Dipolar exchange quantum logic gate with polar molecules, *Chem. Sci.* **9**, 6830 (2018).
- [7] C. M. Holland, Y. Lu, and L. W. Cheuk, On-demand entanglement of molecules in a reconfigurable optical tweezer array, *Science* **382**, 1143 (2023).
- [8] Y. Bao, S. S. Yu, L. Anderegg, E. Chae, W. Ketterle, K.-K. Ni, and J. M. Doyle, Dipolar spin-exchange and entanglement between molecules in an optical tweezer array, *Science* **382**, 1138 (2023).
- [9] L. R. B. Picard, A. J. Park, G. E. Patenotte, S. Gebretsadkan, D. Wellnitz, A. M. Rey, and K.-K. Ni, Entanglement and iSWAP gate between molecular qubits, *Nature* **637**, 821 (2025).
- [10] D. K. Ruttley, T. R. Hepworth, A. Guttridge, and S. L. Cornish, Long-lived entanglement of molecules in magic-wavelength optical tweezers, *Nature* **1** (2025).
- [11] S. Jandura and G. Pupillo, Time-Optimal Two- and Three-Qubit Gates for Rydberg Atoms, *Quantum* **6**, 712 (2022).
- [12] N. Khaneja, T. Reiss, C. Kehlet, T. Schulte-Herbrüggen, and S. J. Glaser, Optimal control of coupled spin dynamics: design of nmr pulse sequences by gradient ascent algorithms, *Journal of Magnetic Resonance* **172**, 296 (2005).
- [13] P. Virtanen, R. Gommers, T. E. Oliphant, M. Haberland, T. Reddy, D. Cournapeau, E. Burovski, P. Peterson, W. Weckesser, J. Bright, S. J. van der Walt, M. Brett, J. Wilson, K. J. Millman, N. Mayorov, A. R. J. Nelson, E. Jones, R. Kern, E. Larson, C. J. Carey, Í. Polat, Y. Feng, E. W. Moore, J. VanderPlas, D. Laxalde, J. Perktold, R. Cimrman, I. Henriksen, E. A. Quintero, C. R. Harris, A. M. Archibald, A. H. Ribeiro, F. Pedregosa, P. van Mulbregt, and SciPy 1.0 Contributors, SciPy 1.0: Fundamental Algorithms for Scientific Computing in Python, *Nature Methods* **17**, 261 (2020).
- [14] M. Bergonzoni, S. Jandura, and G. Pupillo, iswap gate with polar molecules: Robustness criteria for entangling operations, *Phys. Rev. A* **112**, 032621 (2025).

- [15] R. J. P. T. de Keijzer, O. Tse, and S. J. J. M. F. Kokkelmans, Recapture probability for antitrapped rydberg states in optical tweezers, *Phys. Rev. A* **108**, 023122 (2023).
- [16] R. Jozsa, Fidelity for mixed quantum states, *Journal of Modern Optics* **41**, 2315 (1994), <https://doi.org/10.1080/09500349414552171>.
- [17] M. A. Nielsen and I. L. Chuang, *Quantum Computation and Quantum Information: 10th Anniversary Edition* (Cambridge University Press, 2010).
- [18] A. Uhlmann, The “transition probability” in the state space of a *-algebra, *Reports on Mathematical Physics* **9**, 273 (1976).
- [19] G. Giudici, S. Veroni, G. Giudice, H. Pichler, and J. Zeiher, Fast entangling gates for rydberg atoms via resonant dipole-dipole interaction, *PRX Quantum* **6**, 030308 (2025).